

Imaging elastodynamic and hydraulic properties of in-situ fractured rock: An experimental investigation exploring effects of dynamic stressing and shearing

C. Wood¹, P. Shokouhi², P. Manogharan², J. Rivière², D. Elsworth^{3,1}, C. Marone^{1,4}

¹Dept. of Geosciences, Pennsylvania State University, University Park, PA 16802, USA

²Dept. of Engineering Science and Mechanics, Pennsylvania State University, University Park, PA 16802, USA

³Department of Energy and Mineral Engineering, EMS Energy Institute, and G3 Center, The Pennsylvania State University, University Park, PA, USA

⁴Dipartimento di Scienze della Terra, La Sapienza Università di Roma

Key Points:

- Laboratory experiments model field conditions to understand underlying physics of fractured subsurface
 - Active source monitoring reveals complex relationship between elastodynamic and hydraulic properties
 - Dynamic stressing of in-situ fracture results in transient softening, recovery, and permeability enhancement

Abstract

We describe laboratory experiments to elucidate the relationship between nonlinear elasticity and permeability evolution in fractured media subjected to local stress perturbations. This study is part of an effort to image fluid pathways and fracture properties using active-source acoustic monitoring during fluid injection and shear of rough fractures. Experiments were conducted with L-shaped samples of Westerly granite fractured in-situ under tri-axial conditions with deionized water subsequently circulated through the resulting fractures. After in-situ fracturing, we separately imposed oscillations of the applied normal stress and pore pressure with amplitudes ranging from 0.2 to 1 MPa and frequencies from 0.1 to 40 Hz. During these dynamic perturbations an array of piezoelectric transducers continuously transmitted ultrasonic pulses across the fracture to monitor the evolving elastic response. We interpret the resulting evolution of elastic wave properties in the context of elastic nonlinearity and relate the estimated nonlinearity parameters to the relative change in permeability of the fractured media. Fracture roughness is then altered in-situ by shearing, with the generation of breccia and wear products. We document the evolution of permeability and fracture contact stiffness as a function of dynamic stressing and shear offset and discuss our findings in relation to fractures in Earth's crust.

1 Introduction

Dynamic stresses associated with energy production and waste water sequestration (injection, pumping, and transport of supercritical H_2O-CO_2 fluids) are a potentially important contributor to injection-induced seismicity (Healy et al., 1968; Raleigh et al., 1976; Simpson et al., 1988; Sminchak & Gupta, 2003; McNamara et al., 2015; McGarr et al., 2015; Walsh & Zoback, 2015). These perturbations can cause significant changes in the local stress field and poromechanical properties in the subsurface and therefore act as a diagnostic for impending fault reactivation and prospective changes in permeability - among other utilities. Therefore, it is crucial to understand how fluid injection influences the hydromechanical properties of rocks and, in particular, associated fractures. Natural and anthropogenic sources of dynamic perturbation each impact poromechanical properties through similar mechanisms and in similar ways, suggesting uniform controls relating nonlinear stiffness to poromechanical properties. We characterize these

50 dependencies to define the potential to link nonlinear acoustic properties to the evolution
51 of reservoir state and behavior.

52 Empirical evidence from the field and laboratory show that earthquakes and subsequent seismic waves cause transient changes in rock stiffness in the proximity of faults.
53 Specifically, field observations document a sudden reduction in elastic wave velocity associated with co-seismic softening and a post-seismic recovery of rock stiffness that is logarithmic in time e.g., (Brenguier et al., 2008). Similar observations have been made in the laboratory (Elkhoury et al., 2011). Moreover, lab studies using dynamic acousto-elastic testing (Shokouhi et al., 2017), show that ultrasonic wave velocity decreases during dynamic stressing and then recovers with the logarithm of time. These studies show that dynamic strains on the order of 10^{-6} are sufficient to cause the nonlinear elastic effects (Guyer & Johnson, 2009; Riviere et al., 2015).

62 Nonlinear elastic response is sensitive to many fracture properties: geometry, flow
63 pathways, asperity compliance, and friction. Currently, the literature characterizing relationships between elastodynamic and poromechanical response and subsequent recovery is limited (Shokouhi et al., 2020). We present results from sophisticated and highly-constrained laboratory experiments in which we combine the analysis of nonlinear elastodynamic and hydraulic data.

68 The nonlinear behavior of rocks is sensitive to both fine-scale features and second-order constitutive effects, such as fracture apertures (impacting flow pathways, asperity stiffness) and nonlinear stiffnesses (impacted by rate-dependent friction and healing).
69 In order to fully understand the ramifications of dynamic stressing in the subsurface, we
70 need to elucidate the relationship between the elastodynamic and hydro-mechanical properties of fractured rocks.

74 In this paper we build on prior work (Shokouhi et al., 2020) to image acoustic nonlinearity across a fracture using multiple PZT receivers. Also, we relate the average nonlinear acoustic response to fracture permeability as an averaged hydraulic measurement.
75 Another important parameter that we analyze is how the fracture recovers from dynamic
76 stressing. Furthermore, we investigate the effect of shearing on our results, replicating complex natural fractures with heterogeneous roughness and gouge.

80 2 Experimental Setup

81 We conducted laboratory experiments in a true triaxial configuration using frac-
 82 tured granite samples in-situ while simultaneously measuring flow rate and nonlinear elas-
 83 tic properties. Samples of Westerly granite were cut into L-shape blocks (69 x 45 x 50
 84 x 26 mm, Figure 1) with 3 mm deep notches on the top and base to guide the evolution
 85 of planar fractures driven by shear loading to failure. The L-shape is used for maintain-
 86 ing constant nominal contact area during both initial fracture then shear. Our samples
 87 were saturated with deionized water and then placed between steel loading platens with
 88 embedded piezoelectric transducers. The P-polarized lead-zirconate transducers (PZTs)
 89 from APC International Ltd. are 6.5 mm in diameter, with a center frequency of 500 kHz.
 90 The PZTs are epoxied in blind holes 4 mm from the rock sample (Figure 1). The load-
 91 ing platens contain internal conduits to provide a line source of fluid at either end of the
 92 fracture plane. Fluid access at both ends of the fracture was via a narrow channel (45
 93 x 1 mm) fitted with sintered porous fits (permeability $\approx 10^{-14} \text{ m}^2$) and fed by five 1.6-
 94 mm diameter holes. Deionized water was pumped through the fracture at constant pres-
 95 sure drop using independent high speed servo-controllers for both inlet and outlet pres-
 96 sure (Figure 1).

97 The experimental apparatus consists of a stiff load frame and two hydraulic pis-
 98 tons capable of applying force in either displacement- or load-control mode and a pres-
 99 sure vessel with independent control of pore and confining pressures. Applied forces are
 100 measured using custom-built, beryllium-copper strain-gauge load cells mounted on each
 101 loading piston. The load cells have an amplified output of $\pm 5 \text{ V}$ with an accuracy of ± 5
 102 N and are calibrated with a Morehouse proving-ring. Displacements are measured with
 103 direct-current displacement transducers (DCDT), with an accuracy of $\pm 0.1 \mu\text{m}$. Con-
 104 fining pressure was created using a food-grade heat transfer oil (XCELTERM 600, Radco
 105 Industries). A linear variable differential transformer was attached to the sample inside
 106 the pressure vessel to accurately ($\pm 0.1 \mu\text{m}$) measure changes in fracture aperture. Pres-
 107 sure intensifiers fitted with LVDTs and pressure transducers were used to control the con-
 108 fining pressure and the internal upstream and downstream fluid pressures.

109 Each axis of loading is independently servo-controlled and all stresses, strains, fluid
 110 pressures and fluid volumes were recorded with a $\pm 10 \text{ V}$, 16-channel 24-bit analog-to-
 111 digital converter at 10 kHz and averaged to sampling rates of 100 Hz or 1 kHz. Fluid

flow across the fracture was measured using upstream and downstream pore-pressure intensifiers and the permeability was subsequently calculated. Active ultrasonic data were recorded using a VantageTM Research Ultrasound (Verasonics) system. We use broadband (0.02-2 MHz) PZTs (APC International Ltd. 6.35 diameter compressional crystals), which were successively pulsed every 1 ms on the transmitting side and recorded at the receiver side with a sampling rate of 25 MHz. The input signal is a half sine with a frequency of 500 kHz. Also, external triggers sent at regular intervals (of order 1 s) by the Verasonics system were recorded by the 24-bit analog-to-digital data acquisition system. This provided a means for synchronizing the fast-sampled “ultrasonic” and lower sampled “poro-mechanical” data. We used these data to measure changes in the permeability and elasticity of the fractured rock samples.

Before commencing each experiment, the samples were installed in the pressure vessel. Once all fluid pressures and solid stresses were applied, the ultrasonic data acquisition was started. The sample was then fractured in-situ by increasing the shear stress at constant normal stress. After fracturing of the sample we locked the vertical piston (no displacement allowed) and executed the dynamic stressing protocol illustrated in Figure 2a while making continuous measurements of fluid flow and ultrasonic properties.

After executing a series of normal stress and pore pressure oscillation protocols, the fractured sample was sheared twice in 4 mm increments (for a total of 8 mm). During shear, acoustic emissions (AEs) were monitored (passive source recording). Subsequent to each shearing step the dynamic stressing protocol was repeated. We incorporated shearing in this investigation to determine its influence on both the nonlinear elastic and flow properties of the fracture. The fracture aperture is changed through shear, in effect, mimicking the complexity of fractured subsurface rock.

2.1 Experimental Procedure

Each experiment commenced with extensive sample preparation in which the Westerly granite was cut and notched, sealed in a latex jacket, and then placed inside the pressure vessel. The latter was filled with confining fluid before a horizontal stress of 20 MPa was applied. Confining fluid pressure was slowly increased to 15 MPa afterwards. We then applied pore pressure: inlet ($P_{pA} = 4$ MPa) and outlet ($P_{pB} = 2$ MPa). At this state there was no flow because the Westerly granite matrix permeability is very low ($< 10^{-20} \text{ m}^2$)

143 and the confining fluid pressure (around the jacketed sample) is greater than the pore
 144 pressure, preventing the short-circuiting flow of water around the sample.

145 A shear load was then applied with the vertical piston in displacement mode at a
 146 constant rate of $10 \mu\text{m/s}$. Samples fractured in-situ after reaching a critical stress of ≈ 55
 147 MPa, after which we locked the vertical piston. Fluid flow and acoustic emissions were
 148 measured during fracture, but here we focus on dynamic stressing which was implemented
 149 via oscillations of the effective normal stress.

150 Oscillations of the applied normal stress were applied with the horizontal loading
 151 piston at prescribed amplitudes (0.2 to 1 MPa) and frequencies (0.1, 1, 10, 40 Hz). Pore
 152 pressure oscillations were achieved by oscillating P_{PA} at amplitudes of 0.2 to 1 MPa and
 153 frequencies of 0.1, 1, 10 Hz while holding P_{PB} constant. Multiple sets of normal stress
 154 and pore pressure oscillations of varying amplitudes and frequencies were applied to in-
 155 vestigate: (1) repeatability and direct comparison between the two modulated stresses
 156 (normal stress and pore pressure) and (2) amplitude and frequency dependencies of the
 157 measured response. Post-fracture dynamic stressing is plotted in Figure 3d (highlighted
 158 in yellow) and shows the normal stress (red) and pore pressure (blue) oscillations. To
 159 investigate the effect of shearing and resulting changes in fracture aperture and gener-
 160 ated wear material on elastic nonlinearity and permeability, the sample was sheared in
 161 two 4 mm (held at $\sigma_{NS} = 20$ MPa), stages. After each shearing stage the oscillation pro-
 162 tocol was applied to the sample. Initially, the in-situ fracture was quite rough with fines
 163 throughout, but the effect of shear reduces and changes this roughness; the old contacts
 164 were broken and new contacts formed, changing the extent to which the two halves of
 165 the fracture were mated. Throughout shear the size, shape, and amount of wear prod-
 166 ucts, or fines, continuously evolves and likely has a complicated effect on fluid flow. These
 167 measurements allow investigation of how fracture aperture is related to the elastodynamic
 168 and hydromechanical properties.

169 2.2 Permeability Measurements

170 We measured flow rates independently at the fracture inlet (Q_A) and outlet (Q_B)
 171 using the outputs of LVDTs on the pressure intensifiers. After verifying the steady state
 172 flow condition ($Q_A - Q_B \leq 5\%$), Darcy's law was used to calculate permeability k :

$$173 k = \frac{\mu L}{S} \frac{Q}{\Delta P_P} \quad (1)$$

174 where $Q = \frac{1}{2}(Q_A+Q_B)$ is the average flow rate ($\frac{m^3}{s}$), μ is the fluid viscosity ($10^{-3} Pa \cdot s$) at $20^\circ C$, L is the flow path given by the length of the sample (50 mm) and S is the
 175 cross sectional area perpendicular to the flow path ($45 \times 26 mm^2$). Specifically, k is the
 176 bulk permeability, that is, the permeability of the surrounding rock matrix (on order of
 177 $10^{-21} m^2$) and of the fracture. Alternative calculations of permeability are valid (Zhang
 178 et al., 2017; Ishibashi et al., 2018), however we are interested in relative changes in per-
 179 meability in response to dynamic stressing, rather than the absolute value of fracture
 180 permeability.
 181

182 2.3 Ultrasonic Measurements: Active Source

183 Ultrasonic waves transmitted through the fracture were recorded continuously in
 184 each experiment. Half-cycle sinusoidal pulses with an amplitude of 40 V and center fre-
 185 quency of 500 kHz were emitted consecutively from each transmitting transducer (9 piezo-
 186 electric discs arranged in a 3×3 matrix embedded within the right-hand loading platen
 187 in Figure 1b) with a pulse repetition frequency of 100 Hz or 1000 Hz during the low and
 188 high frequency (≥ 10 Hz) stress oscillations, respectively. The waveforms were ampli-
 189 fied (~ 40 dB) and recorded for all the receiving transducers (12 piezoelectric discs ar-
 190 ranged in a 4×3 matrix embedded within the left-hand loading platen in Figure 1b).
 191 In this study we utilized 1 transmitter and 3 receivers.

192 3 Results

193 We combine ultrasonic data, strain measurements, and permeability to document
 194 the nonlinear elastodynamic response and poromechanical effects of dynamic stressing.
 195 Here, we draw from an extensive set (>10) of experiments, calibrations, and tests to fo-
 196 cuse on data from two distinct experiments with a range of stressing amplitudes and fre-
 197 quencies.

198 3.1 Nonlinear elastodynamic and hydraulic responses

199 Linear elasticity does not adequately describe the behaviour of rocks. Even undam-
 200 aged rocks exhibit a range of nonlinearity due to a variety of structural features such as
 201 microcracks and soft grain boundaries (Riviere et al., 2015). When fractured or dam-
 202 aged, the nonlinearity of the rock is further affected by contact acoustic nonlinearity at

203 fracture interfaces. The characteristic responses to dynamic stressing (transient softening,
 204 velocity modulation, and slow recovery) as shown in Figure 5, are indicative of non-
 205 linear mesoscopic elasticity (Guyer & Johnson, 2009) and highly informative on rock mi-
 206 crostructure, fractures, and intergrain contacts. Crucially, these are the features that also
 207 control the hydraulic properties of rock.

208 Through our active source ultrasonic monitoring we characterize the elastodynamic
 209 properties of the fractured Westerly granite by quantifying its response to dynamic stress-
 210 ing. Figure 5 demonstrates typical recorded elastodynamic and hydraulic responses to
 211 a 1 Hz, 1 MPa normal stress oscillation in experiment p4966. We characterize the elas-
 212 todynamic response with three parameters to describe the nonlinearity, $\Delta c/c_0$, dc/c_0 ,
 213 and $\Delta A/A_0$. We observe steady-state wave velocity c_0 before dynamic stressing which
 214 causes an immediate reduction followed by a further transient decrease. Wave velocity
 215 recovers to a new steady-state value that we quantify as Δc . The RMS wave amplitude
 216 is calculated in the time domain in a window comprising the first arrived p-wave, related
 217 to fracture stiffness. Dynamic stress oscillations result in a sudden decrease in amplitude
 218 relative to the initial value A_0 to a new temporary non-equilibrium state. Therefore, both
 219 $\Delta c/c_0$ and $\Delta A/A_0$ represent nonlinear ratios that demonstrate the transient effect of dy-
 220 namic loading on fracture stiffness, for a range of stress amplitudes and frequencies. Al-
 221 though RMS amplitude can be extracted from our data, that is not the main focus of
 222 this paper, but some results are reported in the Supplemental Materials. Another non-
 223 linearity parameter that we identify is modulation of the wave velocity, dc , during os-
 224 cillations at frequencies that are harmonics of the driving frequency. This quantity rep-
 225 resents the average amplitude of wave velocity modulations during dynamic perturba-
 226 tions after the system reaches a non-equilibrium steady-state. Finally, after being stressed,
 227 the fractured rock exhibits long-term “recovery” trending toward the initial c_0 value, in
 228 which the wave velocity or amplitude evolves to a new steady state. The wave velocity
 229 evolution from post-oscillation to initial c_0 is well described by a logarithmic function
 230 of the form $c = p_1 \log t + p_2$, where p_1 is the slope (recovery rate) \dot{c} and p_2 is the in-
 231 tercept.

232 We also measure the evolution of permeability due to dynamic stressing and cor-
 233 relate it with nonlinear elasticity. In our experiments, elastic waves propagate orthog-
 234 onal to the fracture plane and their amplitude, phase and speed depend on the fracture
 235 stiffness that is modulated by aperture. Hydraulic measurements, comparing inlet and

outlet fluid flow across the fracture plane, tell a similar story; permeability and transmissivity reveal changes in fracture aperture. The stress-induced changes in permeability are captured by two parameters: (1) The transient change in permeability $\Delta k/k_0$ defined as the %-change due to the imposed normal stress or pore pressure oscillations, normalized by the pre-oscillation permeability k_0 as illustrated in Figure 5c (Candela et al., n.d.) and (2) the logarithmic rate of permeability recovery after the transient increase \dot{k} where $k = q_1 \log t + q_2$, where q_1 is the slope (recovery rate) and q_2 is the intercept. Figure 5 shows the pre-oscillation permeability k_0 and the post-oscillation permeability $k = k_0 + \Delta k$ calculated by averaging the measured values over 10- and 1-s time windows. Calculation discontinuities in permeability measurements shown in Supplemental Figure 1 correspond to times for which inlet/outlet flow rate difference exceeds the 5% threshold that we impose to ensure steady state flow. Permeability during dynamic stressing is indeterminate because there is no steady-state flow and the diffusion time across the fracture is slower than the higher oscillation frequencies (10 and 40 Hz).

To better illustrate how the elastodynamic and hydraulic properties of fractured rock change in response to dynamic perturbation we show an excerpt from the post-fracture stage of experiment p4975 in Figure 6. Figure 6 demonstrates how the inlet and outlet flow rates evolve during a 0.1 Hz normal stress oscillation; three colorbars highlight zoomed cycles in Figure S4. Note the clear evidence of compression and tension in the fracture normal displacement with increased and decreased normal stress (Figure 7). The inlet Q_A flow rate is in phase with the imposed stressing, but the outlet flow Q_B is 180° out of phase and of a much smaller magnitude than that of the inlet; furthermore, the amplitude trends are modulated throughout the oscillation. For sufficiently long duration stressing the wave velocity modulations reach a steady-state. These observations demonstrate the magnitude of changes we are characterizing and also reinforce that the fracture is continuously evolving during the dynamic perturbations; contacts undergo compression and tension resulting in changing fluid flow paths along the fracture. In subsequent subsections we discuss how nonlinear elastodynamic and hydraulic parameters $\Delta c/c_0$, $\Delta k/k_0$, dc/c_0 , and $\Delta A/A_0$ vary with normal stress and pore pressure oscillation amplitudes and frequencies. We also discuss how these results are affected by shearing for both experiments p4966 and p4975.

267 **3.2 Dynamic Stress-induced Changes in Permeability and Wave Veloc-**
 268 **ity**

269 One hypothesis driving our work is that transient elastic softening and nonlinear
 270 elasticity can provide information about rock fracture properties via dynamic stressing.
 271 A corollary is that changes in fracture aperture cause both changes in permeability and
 272 elasticity. A more complete understanding of both physical phenomena is important for
 273 understanding processes that control energy production from, and waste storage in, the
 274 subsurface. In this section, we report and compare the stress amplitude and frequency
 275 dependencies for both sets of parameters.

276 The dependency of $\Delta k/k_0$ on the amplitude of normal stress and pore pressure os-
 277 cillations is shown in Figure 7, which additionally differentiates the order in which the
 278 1 Hz oscillations sets were imposed. We observe in experiments p4966 and p4975 fairly
 279 similar $\Delta k/k_0$ results for the post-fracture case. This is not entirely surprising because,
 280 although these experiments pertain to different samples/fractures, both samples are West-
 281 erly granite and the same loading conditions were used to produce approximately pla-
 282 nar fractures resulting in presumably similar apertures and amounts of fragmentation.
 283 Interestingly, this similarity deteriorates especially for pore pressure oscillations after the
 284 first shear phase of the experiments. After shearing the fractures (5 mm in p4966 and
 285 4 mm in p4975) fragmented wear products develop at the interface, which inevitably com-
 286 plicated flow – clogging and unclogging during the pore pressure oscillations such that
 287 wear material was dislodged from certain parts of the fracture or lodged in other parts.

288 Compared to dynamic stressing via pore pressure, permeability $\Delta k/k_0$ is relatively
 289 unaffected by oscillations of the applied normal stress oscillations for post-shear cases.
 290 This suggests that gouge material generated during shear is not mobilized to the degree
 291 it is by pore pressure, perhaps because pore fluids are more effective in moving gouge
 292 material and clogging/unclogging flow paths. This mechanism is not fully understood
 293 but likely plays a significant role in this complicated process.

294 We observe that the relative permeability change $\Delta k/k_0$ generally scales with the
 295 amplitude of the 1 Hz normal stress oscillation post fracture and pore pressure oscilla-
 296 tions and that the order in which oscillations were applied have an effect on the perme-
 297 ability enhancement. There are cases especially for post-shear oscillations where small
 298 oscillation amplitudes ($< 0.5 \text{ MPa}$) result in a modest reduction in permeability for nor-

299 mal stress oscillations, but can result in relatively larger reductions for pore pressure os-
 300 cillations. Despite scatter, fairly similar relationships are observed for the two separate
 301 experiments.

302 The sequenced order of oscillations does not necessarily correlate to a specific per-
 303 meability enhancement or reduction, but does have an effect on the overall results. This
 304 is most likely due to the fact that the pore pressure and normal stress oscillations do not
 305 strictly alternate, although the order is consistent in post-fracture, post-shear 1, and post-
 306 shear 2 parts of the experiments as shown in Figure 3d

307 The relative change in velocity $\Delta c/c_0$ for the direct transmitter-receiver pair as a
 308 function of 1 Hz normal stress and pore pressure oscillation amplitudes are plotted in
 309 Figure 8. As expected (Riviere et al., 2015), we observe an increasing velocity drop (more
 310 negative $\Delta c/c_0$) with oscillation amplitude for both normal stress and pore pressure.

311 In this measure of fracture nonlinearity there is a clearer trend between oscillation
 312 order and magnitude, for this transmitter-receiver path. Normal stress oscillations for
 313 the post-fracture case exhibit less nonlinearity compared to subsequent oscillation sets.
 314 The degree of nonlinearity from pore pressure oscillations, though linear with oscillation
 315 amplitude, remains relatively unchanged with shearing.

316 The effect of shear on fracture nonlinearity is more obvious for pore pressure os-
 317 cillations and rather scattered for applied normal stress oscillation sets. Interestingly,
 318 the nonlinearity relationship with amplitude barely changes with amount of shear for p4975;
 319 though for p4966, shearing the fracture increases the nonlinearity. However, for applied
 320 normal stress, successive shear scatters the trend we observe in post-fracture sets, pre-
 321 sumably deriving from dramatic changes in asperity contacts that occur with progres-
 322 sive shear displacement.

323 3.3 Spatial Variations of the Nonlinear Elastodynamic Response

324 The elastic response ($\Delta c/c_0$) presented in Figure 8 corresponded to a single pair
 325 of transducers. Figure 9 shows a coarse view of the nonlinear elastodynamic response
 326 across the fracture as a function of applied oscillation amplitude. Note that data point
 327 shape corresponds to oscillation frequencies. The direct path sensor, blue PZT in Fig-
 328 ures 9 – 10) shows a general trend of increasing nonlinearity with stress oscillation am-

329 plitude and frequency, in both experiments. The other sensors measure more scatter and
330 also more linearity in the case of the bottom sensor of p4975. The shearing reduces non-
331 linearity (direct pair) and modestly increases nonlinearity (top sensor path), but does
332 not have an overall coherent trend for both experiments and all increments of shear. The
333 response to pore pressure oscillations, Figure 10, shows more coherent results as com-
334 pared to applied normal stress. Again, there is a general trend in increasing nonlinear-
335 ity with amplitude and oscillation frequency; it is interesting that the bottom receiver
336 path exhibits markedly lower nonlinearity. Furthermore, there is much more similarity
337 in results for the separate experiments than observed in the normal stress oscillations.
338 Another important observation is that shearing has little effect on the magnitude of non-
339 linearity for pore pressure oscillations.

340 The scatter in these results is not unexpected given that the fracture has a hetero-
341 geneous aperture and irregularly distributed wear products, especially following the ap-
342 plication of shear displacement. It is conceivable that shear increases the aperture in some
343 locations, which could be filled with wear/gouge material or remain empty, while other
344 parts of the fracture aperture could be closed. These possibilities may be partially re-
345 sponsible for the complicated behavior we observe.

346 To further our understanding of the coupling between elastodynamic and hydraulic
347 response to dynamic stressing, we investigate the spatial variations of the elastic response
348 along the fracture by analyzing all available transmitter-receiver pairs measurement of
349 wave velocity (Figures 9 – 10). Figure 11 relates permeability changes $\Delta k/k_0$, an hydraulic
350 measurement averaged over the fracture plane, to the change in wave velocity $\Delta c/c_0$ av-
351 eraged across all receiver locations. The data point shapes again correspond to the os-
352 cillation frequencies and their sizes correspond to oscillation amplitude. The main ob-
353 servation for the post-fracture oscillation sets is that relative changes in permeability and
354 wave velocity are correlated. That is to say, larger normal stress or pore pressure oscil-
355 lation amplitudes and frequencies produce larger transient softening and permeability
356 enhancement. Overall, shear weakens this relationship, reducing the amount of nonlin-
357 earity and permeability enhancement for both methods of dynamic stressing. Though,
358 in the case of normal stress oscillations, the relationship with amplitude and frequency
359 still exists, but the overall slope decreases due to shear displacement.

We conjecture that the nature of the correspondence between nonlinear elastodynamic and hydraulic properties of fractured rock depend not only on fracture aperture change due to stressing but also on clogging mechanisms. During both types of dynamic stressing fracture flow conduits are likely to be clogged/unclogged in a complicated fashion, resulting in mobilization of gouge material (generated from in-situ fracture and subsequent shear displacement) and permeability enhancement/reduction. This has also been observed in previous studies of Berea sandstone (Elkhoury et al., 2011; Candela et al., n.d., 2015). However unlike in previously reported studies, we observe permeability enhancement for both normal stress and pore pressure oscillations (for amplitudes > 0.5 MPa). Thus, fracture aperture change from stressing and clogging mechanisms can not adequately explain the rich underlying physics.

371 3.4 Wave Velocity Modulation

The direct effect of dynamic stressing is an instantaneous modulation in wave velocity at harmonic frequencies of the driving frequency. We denote the mean velocity amplitude as dc (e.g., Figure 5). The relative change in average velocity oscillations dc/c_0 is a proxy for the nonlinear parameter β , estimated from the second harmonic (e.g., (Guyer & Johnson, 2009; Riviere et al., 2013, 2015)). We observe a monotonic relationship between the magnitude of dc/c_0 and oscillation amplitude for both rock samples (Figure 12).

There is a consistent trend that subsequent oscillation sets decrease the magnitude of nonlinearity of dc/c_0 for normal stress modulation. Pore pressure oscillations exhibit little to no change through subsequent repetitions, except for larger driving amplitudes. Shearing the fracture generally decreases the measured nonlinearity, especially for experiment p4966 (Figure 12). The trend is not as strong for p4975, where little to no change in dc/c_0 nonlinearity is observed after the first shear increment. Then, after the second shear, pore pressure oscillations interestingly increase the nonlinearity. We posit that the two types of dynamic stressing activate two different mechanisms: (1) opening/closing of pore throats from normal stress oscillations and (2) directly dislodging and mobilizing fines along the fracture from pore pressure oscillations. This is consistent with our observations of other nonlinearity parameters.

390 3.5 Permeability and Wave Velocity Recovery from Dynamic Stressing

391 The long term evolution of permeability and wave velocity reveal the extent to which
 392 fines are transported along the fracture and how fracture asperities recover from dynamic
 393 stresses. We discriminate fitted slopes (see section 3.1) if the R^2 value is below the mean
 394 of the respective experimental run. We observe trends, particularly in experiment p4975,
 395 where the permeability recovery linearly decreases with pore pressure oscillations (see
 396 insets of Figure 13). The permeability recoveries from normal stress oscillations are mi-
 397 nuscule and slopes have very low goodness of fit and do no report the data. These re-
 398 sults suggest that the opening and closing mechanism of the fracture from normal stress
 399 oscillations is ineffective in unclogging fines to migrate along the fracture. Large ampli-
 400 tude pore pressure oscillations are more effective in mobilizing the fines, thus allowing
 401 for a more rapid recovery to its initial state. Furthermore, there is little effect of order
 402 of oscillation for both stimulation methods.

403 Shearing the fracture does not result in slower permeability recovery rates in re-
 404 sponse to pore pressure oscillations, see Post - Shear 1 and 2 from Figure 13. Because
 405 there is an increase in the accumulation of fines from shearing, the permeability recov-
 406 ers slower in response to pore pressure oscillations. We posit that the wear material is
 407 comminuted as a result of subsequent shearing and normal stress oscillations, is trans-
 408 ported along the fracture during the pore pressure oscillations, and impedes a recovery
 409 from the transient change.

410 The wave velocity recovery rate \dot{c} for the direct transmitter-receiver pair as a func-
 411 tion of 1 Hz normal stress and pore pressure oscillation amplitudes is plotted in Figure
 412 14. We observe faster recovery with oscillation amplitude for both normal stress and pore
 413 pressure. In the post-fracture phase, there is a noticeable effect of order of σ_{NS} oscil-
 414 lations on recovery rate; later oscillations exhibit smaller magnitude of \dot{c} , which demon-
 415 strates detectable damage to the fracture asperities from the first oscillation set.

416 The effect of shear on fracture \dot{c} is a decrease in the magnitude of recovery rate and
 417 a flattening of the relationship between \dot{c} and oscillation amplitude for both perturba-
 418 tion methods. There is perhaps a complex effect from deformation of fracture asperities
 419 and the granular wear material that inhibit the recovery from the transient response to
 420 dynamic stressing.

421 Figure 15 relates the wave velocity recovery rate \dot{c} averaged over all receiver loca-
 422 tions to permeability changes \dot{k} , a hydraulic measurement across the fracture. The main
 423 observation \dot{c} and \dot{k} are uncorrelated for normal stress oscillations, but are more corre-
 424 lated for pore pressure oscillations in the post-fracture phase, though sparse. Also, there
 425 does not seem to be obvious scaling of frequency with the the relation between \dot{c} and \dot{k} .
 426 Overall, shearing the fracture decreases both the velocity and permeability recovery rates
 427 for pore pressure oscillations, especially in experiment p4975.

428 4 Conclusions

429 We report laboratory experiments to determine the effects of dynamic stressing and
 430 shearing on elastodynamic and hydraulic properties of fractured rock. Processes control-
 431 ling fluid flow in reservoirs, including subsurface waste disposal, and hydrocarbon pro-
 432 duction derive from a complex interplay of these properties. Monitoring in-situ fractures
 433 with active source ultrasonic transmission and fluid permeability during dynamic stress-
 434 ing driven by both total stresses and fluid pressures reveals the complex relation between
 435 elastodynamic and hydraulic properties.

436 In response to oscillations of effective normal stress, Westerly granite samples ex-
 437 hibit characteristic transient softening, acoustic velocity fluctuations, and slow recovery,
 438 informing us about microstructure and contact mechanics. We observe that large am-
 439 plitude and high frequency oscillations generally increase permeability, with pore pres-
 440 sure oscillations producing the largest enhancement of permeability. Furthermore, we
 441 document spatial variability in elastodynamic properties across the fractures, revealing
 442 the effect of variations in fracture aperture and contact stiffness. Shearing generally de-
 443 creases this nonlinearity parameter for both oscillation modes. The exact underlying physics
 444 remain unclear of how fracture asperity and aperture changes resulting from dynamic
 445 stressing and clogging mechanisms account for these results. However, our observations
 446 do suggest that the two types of dynamic stressing activate two different mechanisms;
 447 aperture change dominates during applied normal stress oscillations and unclogging dom-
 448 inates during pore pressure oscillations.

449 Future experiments with pre-fractured samples will include characterization of sur-
 450 face roughness with high-resolution profilometry to better constrain the underlying me-
 451 chanics of aperture and permeability change. Furthermore, we will develop methods to

452 collect fine gouge material generated from in-situ fracturing and shearing in the down-
 453 stream pore pressure lines in an attempt to quantify the degree to which unclogging mech-
 454 anisms are responsible for the results we observe.

455 **Acknowledgments**

456 Experimental and data analysis assistance from Benjamin Madara and Jiang Jin, respect-
 457 fully, was invaluable. Technical assistance from Steven Swavely is gratefully acknowledged.
 458 This work was fully supported by a grant from DOE Office of Basic Energy Science (DE-
 459 SC0017585) to PS. CM acknowledges support from European Research Council Advance
 460 Grant 835012 (TECTONIC) and US Department of Energy grants DE-SC0020512 and
 461 DE-EE0008763

462 **References**

- 463 Brenguier, F., Campillo, M., Hadzioannou, C., Shapiro, N. M., Nadeau, R. M.,
 464 & Larose, E. (2008). Postseismic relaxation along the san andreas fault at
 465 parkfield from continuous seismological observations. *Science*, *321*(5895),
 466 1478–1481. Retrieved from <https://science.sciencemag.org/content/321/5895/1478> doi: 10.1126/science.1160943
- 467 Candela, T., Brodsky, E. E., Marone, C., & Elsworth, D. (n.d.). Laboratory evi-
 468 dence for particle mobilization as a mechanism for permeability enhancement
 469 via dynamic stressing.
- 470 Candela, T., Brodsky, E. E., Marone, C., & Elsworth, D. (2015). Flow rate dic-
 471 tates permeability enhancement during fluid pressure oscillations in laboratory
 472 experiments. *Journal of Geophysical Research: Solid Earth*, *120*(4), 2037–
 473 2055. Retrieved from <https://agupubs.onlinelibrary.wiley.com/doi/abs/10.1002/2014JB011511> doi: <https://doi.org/10.1002/2014JB011511>
- 474 Elkhoury, J. E., Niemeijer, A., Brodsky, E. E., & Marone, C. (2011). Laboratory
 475 observations of permeability enhancement by fluid pressure oscillation of in
 476 situ fractured rock. *Journal of Geophysical Research: Solid Earth*, *116*(B2).
 477 Retrieved from <https://agupubs.onlinelibrary.wiley.com/doi/abs/10.1029/2010JB007759> doi: <https://doi.org/10.1029/2010JB007759>
- 478 Guyer, R. A., & Johnson, P. A. (2009). *Nonlinear mesoscopic elasticity: the complex*
 479 *behaviour of rocks, soil, concrete*. John Wiley & Sons.

- 483 Healy, J. H., Rubey, W. W., Griggs, D. T., & Raleigh, C. B. (1968). The
484 denver earthquakes. *Science*, 161(3848), 1301–1310. Retrieved from
485 <https://science.sciencemag.org/content/161/3848/1301> doi:
486 10.1126/science.161.3848.1301
- 487 Ishibashi, T., Elsworth, D., Fang, Y., Riviere, J., Madara, B., Asanuma, H., ...
488 Marone, C. (2018). Friction-stability-permeability evolution of a frac-
489 ture in granite. *Water Resources Research*, 54(12), 9901-9918. Retrieved
490 from <https://agupubs.onlinelibrary.wiley.com/doi/abs/10.1029/2018WR022598> doi: <https://doi.org/10.1029/2018WR022598>
- 491 McGarr, A., Bekins, B., Burkardt, N., Dewey, J., Earle, P., Ellsworth, W., ... Shee-
492 han, A. (2015). Coping with earthquakes induced by fluid injection. *Science*,
493 347(6224), 830–831. Retrieved from <https://science.sciencemag.org/content/347/6224/830> doi: 10.1126/science.aaa0494
- 494 McNamara, D. E., Hayes, G. P., Benz, H. M., Williams, R. A., McMahon, N. D.,
495 Aster, R. C., ... Earle, P. (2015). Reactivated faulting near cushing, ok-
496 lahoma: Increased potential for a triggered earthquake in an area of united
497 states strategic infrastructure. *Geophysical Research Letters*, 42(20), 8328-
498 8332. Retrieved from <https://agupubs.onlinelibrary.wiley.com/doi/abs/10.1002/2015GL064669> doi: <https://doi.org/10.1002/2015GL064669>
- 499 Raleigh, C. B., Healy, J. H., & Bredehoeft, J. D. (1976). An experiment in earth-
500 quake control at rangely, colorado. *Science*, 191(4233), 1230–1237. Retrieved
501 from <https://science.sciencemag.org/content/191/4233/1230> doi: 10.
502 .1126/science.191.4233.1230
- 503 Riviere, J., Renaud, G., Guyer, R. A., & Johnson, P. A. (2013). Pump and probe
504 waves in dynamic acousto-elasticity: Comprehensive description and com-
505 parison with nonlinear elastic theories. *Journal of Applied Physics*, 114(5),
506 054905. Retrieved from <https://doi.org/10.1063/1.4816395> doi:
507 10.1063/1.4816395
- 508 Riviere, J., Shokouhi, P., Guyer, R. A., & Johnson, P. A. (2015). A set of measures
509 for the systematic classification of the nonlinear elastic behavior of disparate
510 rocks. *Journal of Geophysical Research: Solid Earth*, 120(3), 1587-1604.
511 Retrieved from <https://agupubs.onlinelibrary.wiley.com/doi/abs/10.1002/2014JB011718> doi: <https://doi.org/10.1002/2014JB011718>

- 516 Shokouhi, P., Jin, J., Wood, C., Rivière, J., Madara, B., Elsworth, D., & Marone,
517 C. (2020). Dynamic stressing of naturally fractured rocks: On the relation
518 between transient changes in permeability and elastic wave velocity. *Geo-*
519 *physical Research Letters*, 47(1), e2019GL083557. Retrieved from <https://agupubs.onlinelibrary.wiley.com/doi/abs/10.1029/2019GL083557>
520 (e2019GL083557 2019GL083557) doi: <https://doi.org/10.1029/2019GL083557>
- 521 Shokouhi, P., Riviere, J., Guyer, R. A., & Johnson, P. A. (2017). Slow dynamics of
522 consolidated granular systems: Multi-scale relaxation. *Applied Physics Letters*,
523 111(25), 251604. Retrieved from <https://doi.org/10.1063/1.5010043> doi:
524 10.1063/1.5010043
- 525 Simpson, D., Leith, W., & Scholz, C. (1988, 12). Two types of reservoir-induced seis-
526 micity. *Bulletin of the Seismological Society of America*, 78(6), 2025-2040.
- 527 Sminchak, J., & Gupta, N. (2003, 06). Aspects of induced seismic activity and deep-
528 well sequestration of carbon dioxide. *Environmental Geosciences*, 10(2), 81-89.
529 Retrieved from <https://doi.org/10.1306/eg.04040302009> doi: 10.1306/eg
530 .04040302009
- 531 Walsh, F. R., & Zoback, M. D. (2015). Oklahoma's recent earthquakes and salt-
532 water disposal. *Science Advances*, 1(5). Retrieved from <https://advances.sciencemag.org/content/1/5/e1500195> doi: 10.1126/sciadv.1500195
- 533 Zhang, F., Fang, Y., Elsworth, D., Wang, C., & Yang, X. (2017). Evolution of Fric-
534 tion and Permeability in a Propped Fracture under Shear. *Geofluids*, 2017,
535 2063747. Retrieved from <https://doi.org/10.1155/2017/2063747> doi:
536 10.1155/2017/2063747
- 537
- 538

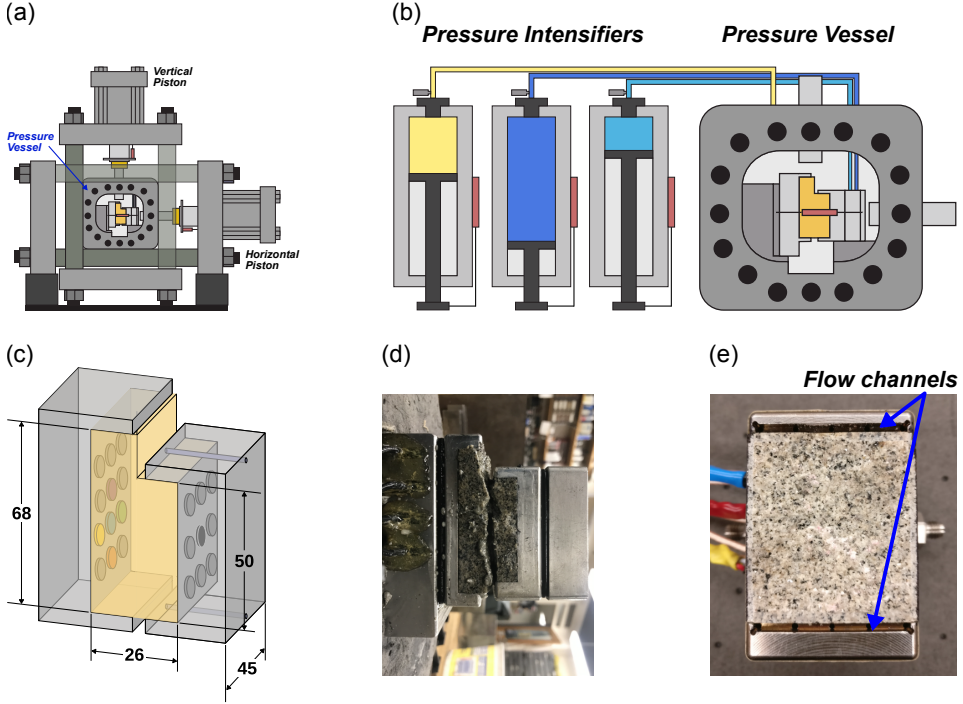


Figure 1. (a) Experiments were conducted in the Penn State Rock and Sediment Mechanics laboratory using the Biaxial Deformation Apparatus (Biax). The Biax has servo-controlled vertical and horizontal pistons and a 10 kHz 24-bit analog to digital data recorder. (b) A pressure vessel is inserted into the Biax to create true triaxial loading. Pressure intensifiers control the confining pressure (P_C) and sample (P_{PA} and P_{PB}) fluid pressures. (c) L-shaped samples of granite were loaded with platens containing piezoelectric transducers (p-polarized). The shorter platen has internal conduits to provide fluid at each end of the fracture plane via narrow channels (45×1 mm). Each channel is covered by a sintered porous frits (permeability $\sim 10^{-14} \text{ m}^2$) and fed by five 1.6 mm diameter holes. The frits ensure homogeneous fluid distribution at each end of the fracture. After securing the sample in the loading platens it is sealed in a latex jacket to separate confining and pore fluids. (d) A photo of the sample after experimentation highlights the degree of roughness resulting from the in-situ fracturing. (e) Post-mortem photograph showing the rough fracture and fluid flow channels.

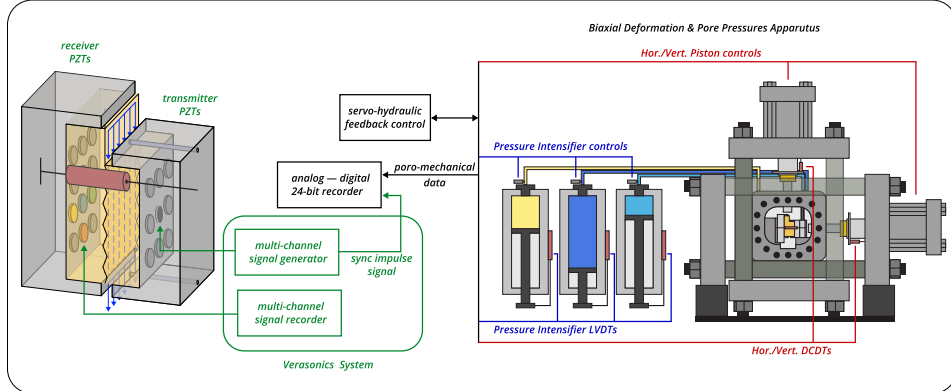


Figure 2. Schematic of the single direct shear configuration with the block diagram showing the main features of the data acquisition system for both the poro-mechanical and ultrasonic data. The Biax consists of two hydraulic pistons capable of applying vertical and horizontal loads in displacement or load control. Forces are measured using custom-built strain-gauge load cells mounted on the displacement rams. The load cells have an amplified output of 5 V with an accuracy of 5 N and are calibrated with a Morehouse proving-ring. Displacements are measured with direct-current displacement transducers (DCDT), with an accuracy of $\pm 0.1\mu m$. Each axis of loading is independently servo-controlled and all stresses, strains, fluid pressures and fluid volumes were recorded with ± 10 V, 16-channel 24-bit analog-to-digital converters at 10 kHz and averaged to sampling rates of 100 Hz or 1 kHz. Fracture permeability was measured using upstream and downstream pore-pressure intensifiers. Active ultrasonic data were recorded using a Vantage TM Research Ultrasound (Verasonics) system. We use broadband (0.02-2 MHz) PZTs (APC International Ltd. 6.35 mm diameter compressional crystals), which were successively pulsed every 1 ms on the transmitting side and the recording rate at the receiver side was 25 MHz. The input signal is a half sine with a frequency of 500 kHz. Also, the Verasonics system sends external triggers at regular intervals (≈ 1 s) that are recorded by the 24-bit analog-to-digital data acquisition system. This allows synchronizing of the ultrasonic data to the poro-mechanical data and then their joint analysis to measure changes in the permeability and elasticity of the fractured rock samples, explained more fully in the signal analysis procedure.

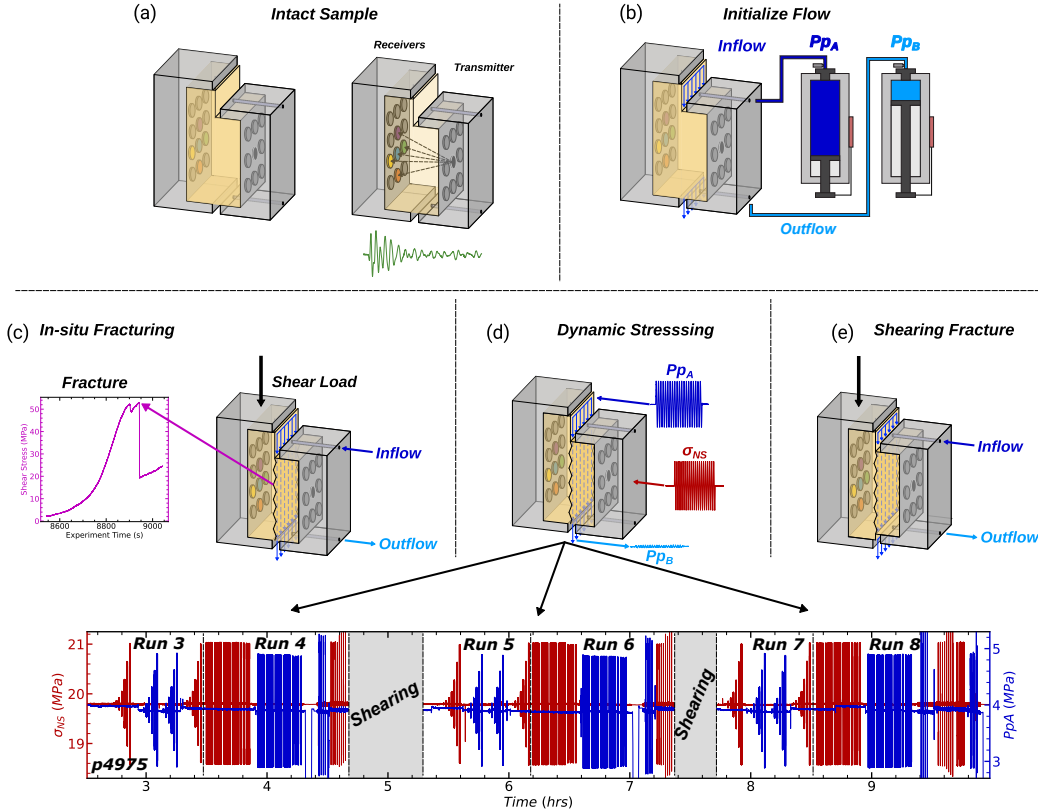


Figure 3. (a) Sketch showing sample dimensions and approximate PZT transmitter - receiver ray paths. (b) Fluid flow and pore pressure with inlet ($P_{PA} = 4$ MPa) and outlet ($P_{PB} = 2$ MPa). (c) Shear stress on the fracture plane was increased by advancing the long end of the L-shaped sample at a constant rate of $10 \mu\text{m}/\text{s}$ while holding the short end in place. Fracture occurred in two stages at ≈ 55 MPa. (d) Sketch showing the oscillation protocol applied to the freshly fractured sample. Multiple sets of P_P and σ_{NS} oscillations of varying amplitude (up to about ± 1 MPa) and frequency (0.1, 1, 10 and 40 Hz) were applied. (e) Fractures were sheared in two stages, each followed by the dynamic stressing protocol.

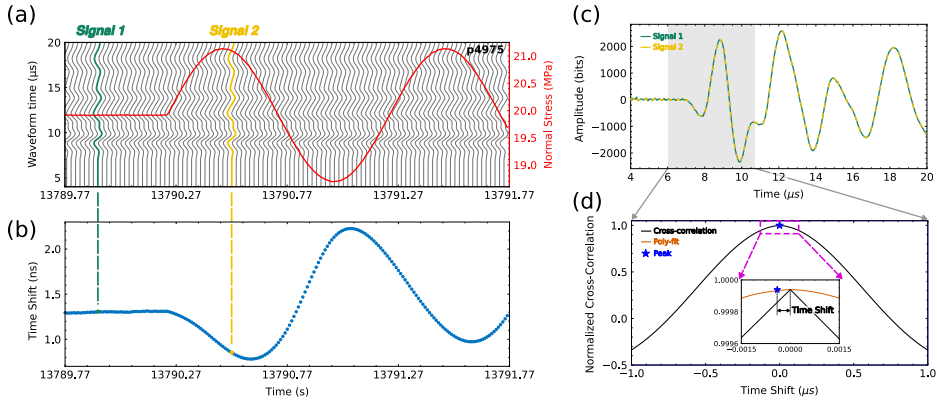


Figure 4. (a) Excerpt from Run 4 of experiment p4966 (see Fig. 3 for context in p4975) shows part of a 1 Hz, 1 MPa normal stress oscillation (red) and the concurrent raw ultrasonic waveforms (grey). The number of waveforms in the waterfall plot has been decimated for clarity. (b) Time shift was calculated by cross-correlating the waveforms with a reference waveform. (c) An example of a reference, unperturbed, waveform (green) and perturbed waveform (dashed yellow) highlights the similarity. (d) The maximum linear correlation between the reference and perturbed waveforms from cross-correlation is used to determine the time shift. The inset shows improvement of time shift calculations with a 2nd order polynomial fitting procedure.

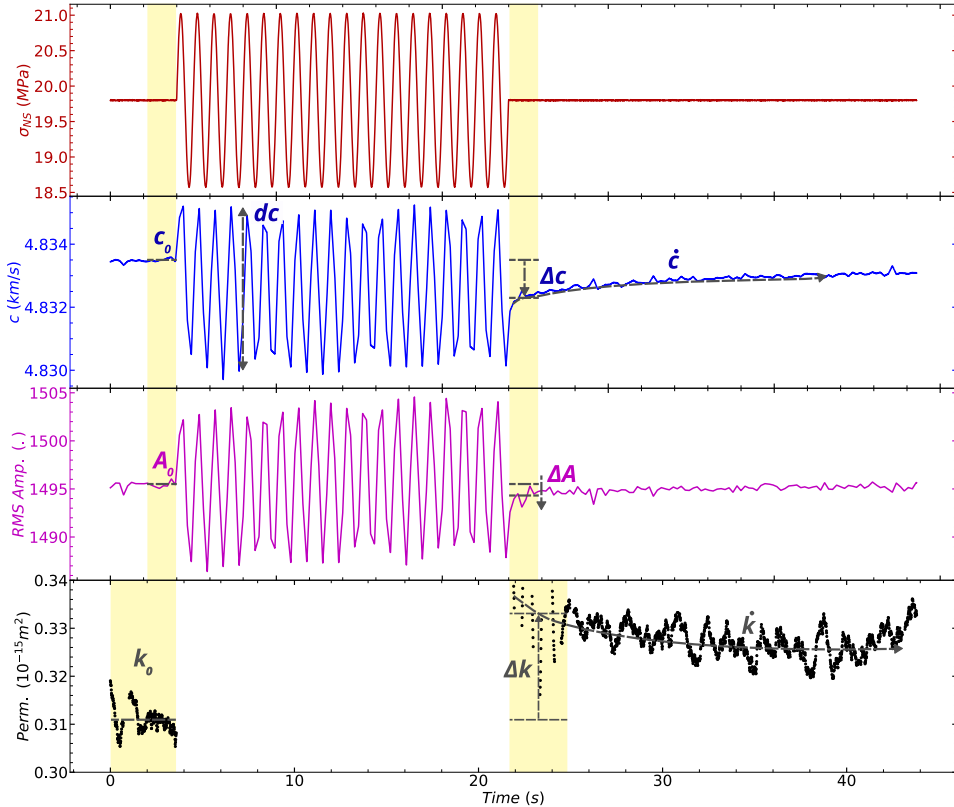


Figure 5. Details of elastodynamic and hydraulic response to dynamic stress oscillation, see Run 4 of p4975 in Fig. 3. Wave velocity and permeability changes are calculated using the measured values before and after oscillations averaged over the time windows indicated by yellow boxes. Permeability measurements are shown only for steady state flow when the inlet/outlet flow rates differ by < 5%. We measure the dynamically induced changes in p-wave velocity (\dot{c}) and permeability (\dot{k}) as well as their changes Δc and ΔA relative to the initial values c_0 and A_0 . Furthermore, we measure the average change in p-wave velocity during dynamic stressing oscillations as dc .

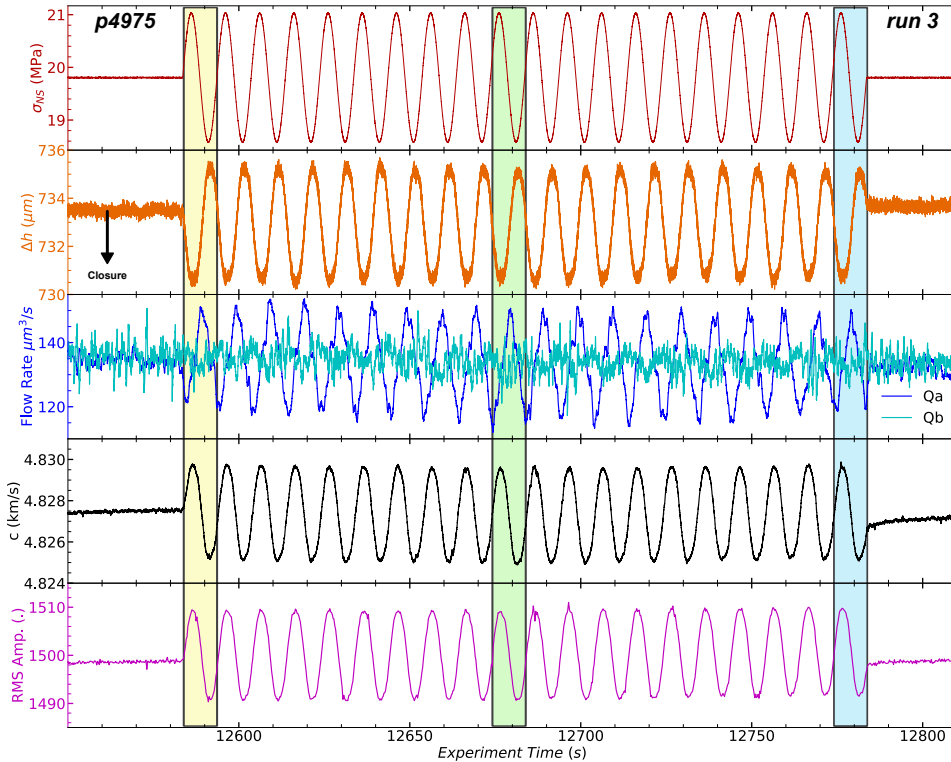


Figure 6. Elastodynamic and hydraulic data for one set of applied normal stress oscillations at a frequency of 0.1 Hz and amplitude of 1 MPa (See Fig. 3). Fracture aperture decreases initially as normal stress increases and then varies in phase with fracture normal stress. Fluid flow data from the fracture inlet (PpA) and outlet (PpB) document the transient response to changes in fracture aperture and stress state. Note that inflow is phase lagged relative to fracture aperture. Elastic wave speed and amplitude are shown for the direct path pair (center transmitter to blue receiver in Figure 2). Three sections are highlighted showing one full cycle in the beginning, middle, and end of the normal stress oscillation.

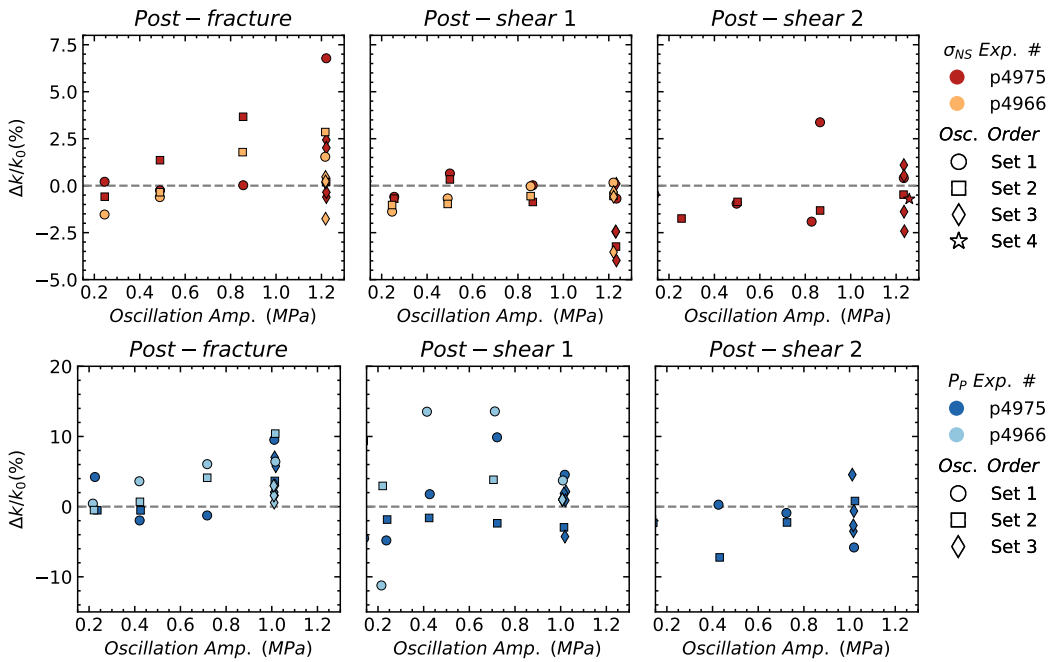


Figure 7. Relative changes in permeability for dynamic stressing via applied normal stress (top row) σ_{NS} and pore pressure (lower row) P_p at 1 Hz. Data are shown for the period just after the fracture formed (post-fracture) and after each increment of shear. Comparing post-fracture results to post-shear we observe a general reduction of permeability enhancement via dynamic stressing with smaller values of $\Delta k/k_0$. Gouge generated from shear is likely clogging flow pathways along the fracture plane. The hypothesized impediment to flow for the post-shear oscillation sets causes a reduction in permeability enhancement, especially for the post-shear 2 oscillation set.

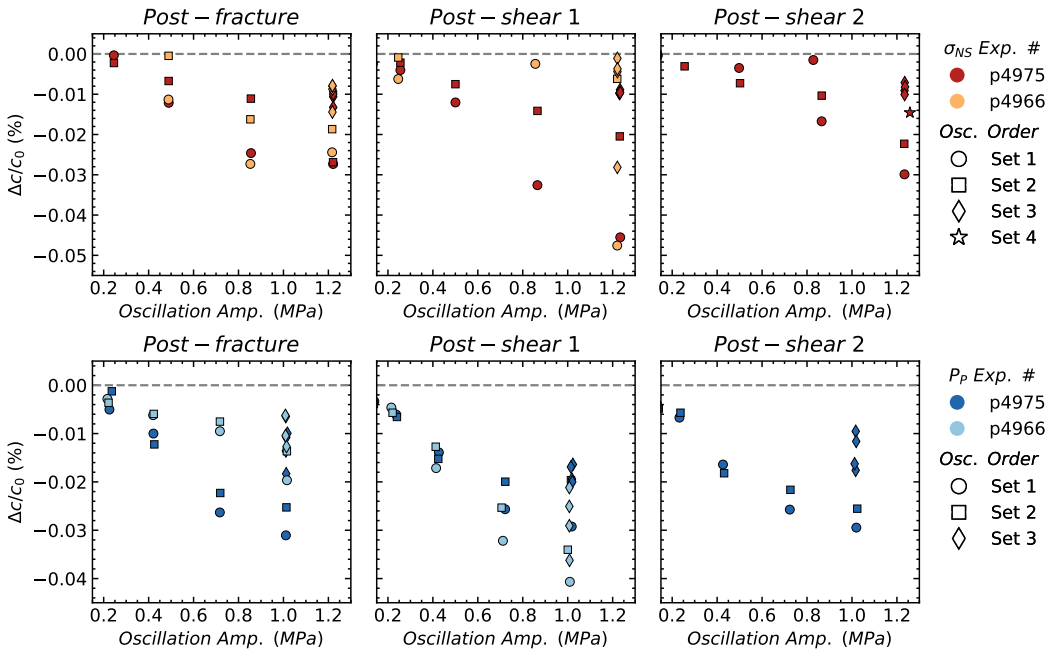


Figure 8. Relative changes in p-wave speed for dynamic stressing via applied normal stress (top row) σ_{NS} and pore pressure (lower row) P_p . Data are shown for the direct transmitter-receiver pair (see Figure 2). Note that the magnitude of Δc increases as a function of oscillation amplitude. Transitioning from post-fracture results to post-shear results, we observe decreased and more scattered nonlinearity.

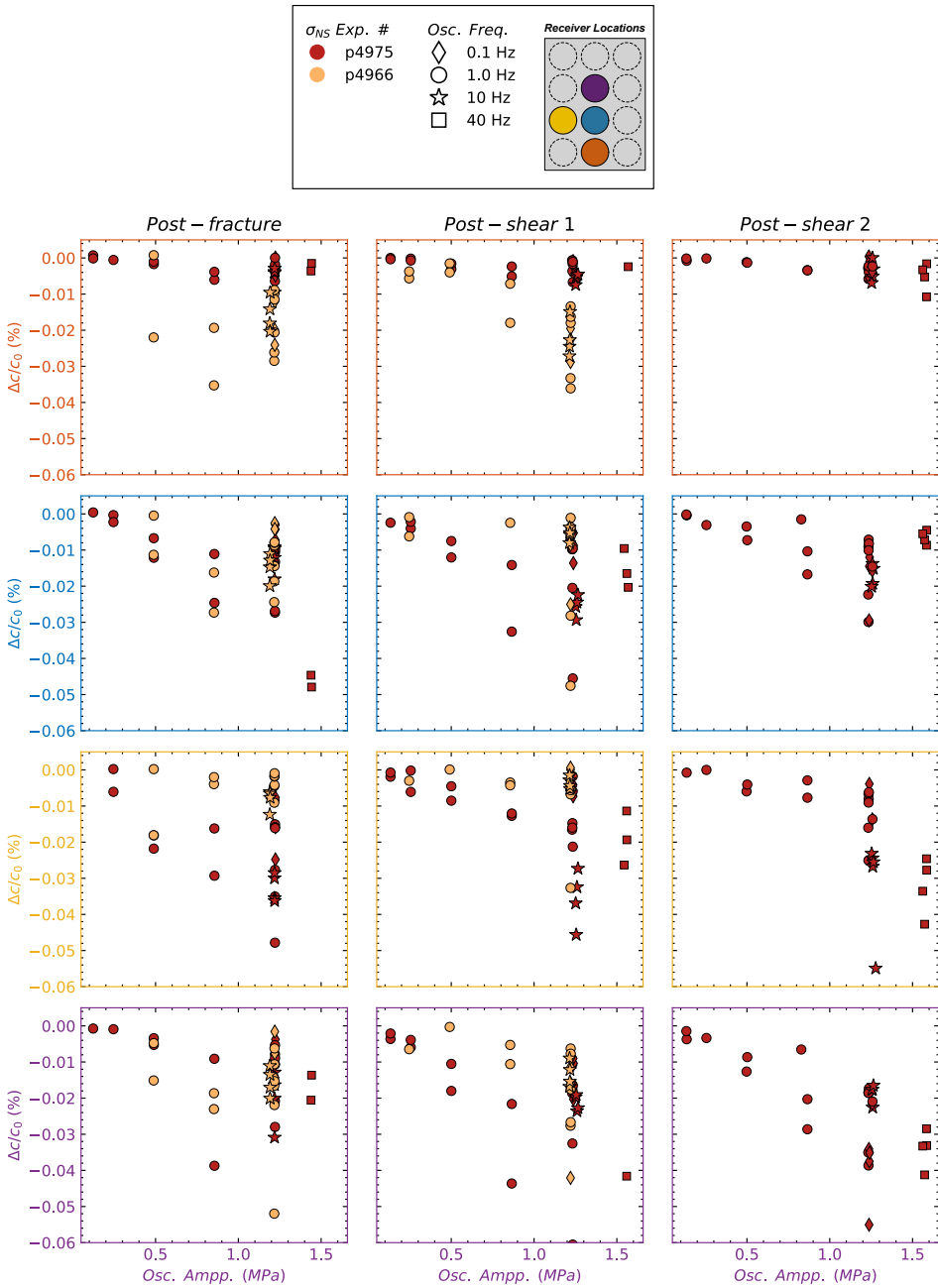


Figure 9. Nonlinearity as a function of σ_{NS} oscillation amplitude for each receiver. Transitioning from post-fracture results to post-shear results, we observe decreasing nonlinearity. The plot colors correspond to PZT receiver locations. These results demonstrate the spatial variability in nonlinear elasticity across the fracture plane and furthermore shows that the two Westerly granite samples exhibit similar responses to the normal stress oscillations.

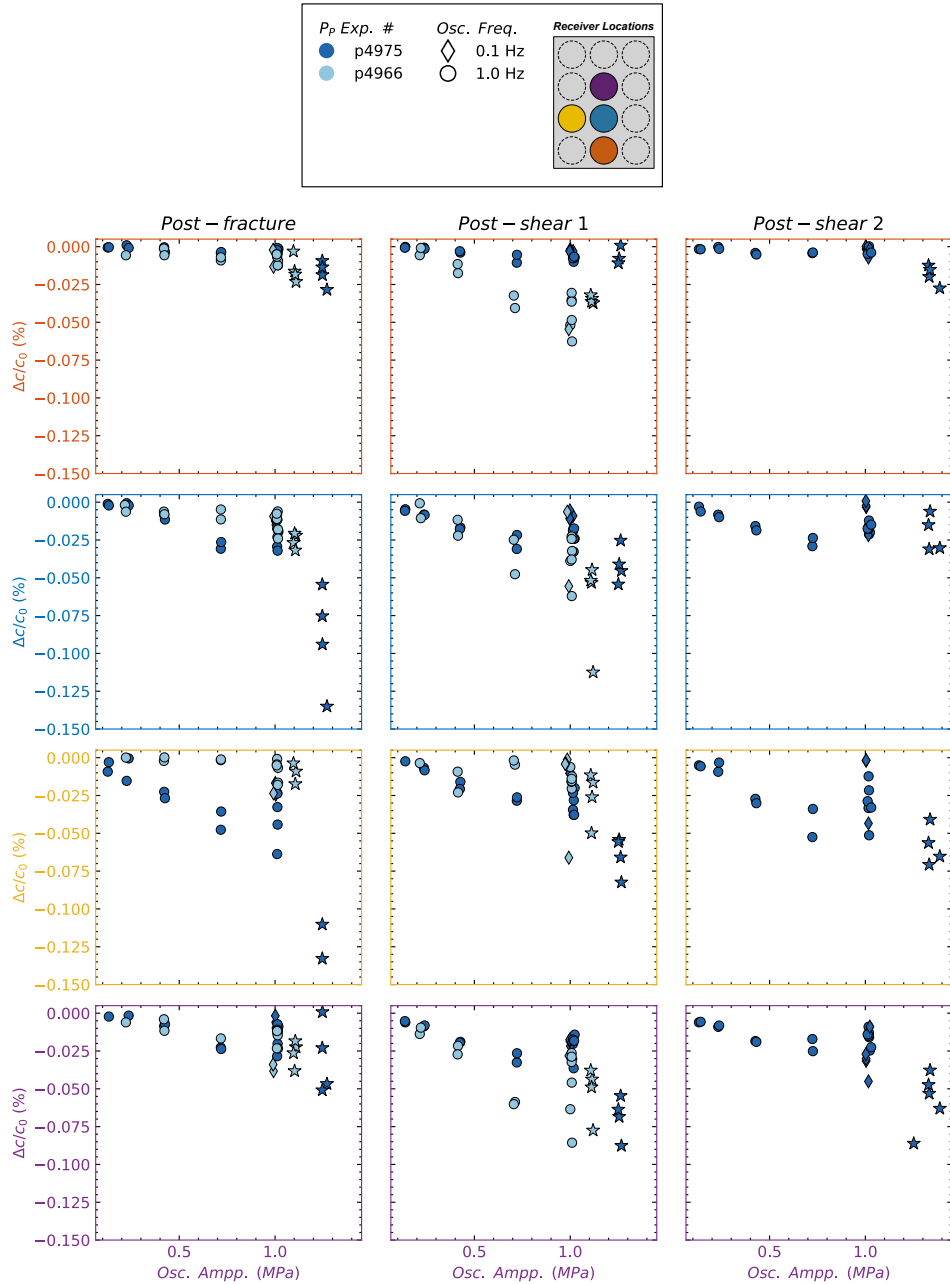


Figure 10. Nonlinearity as a function of pore pressure oscillation amplitude for each receiver.

Transitioning from post-fracture results to post-shear results, we observe decreased nonlinearity. The spatial variability shows that the pore pressure oscillations in some of the receiver locations throughout the experiments cause larger changes in elastic nonlinearity than the normal stress oscillations.

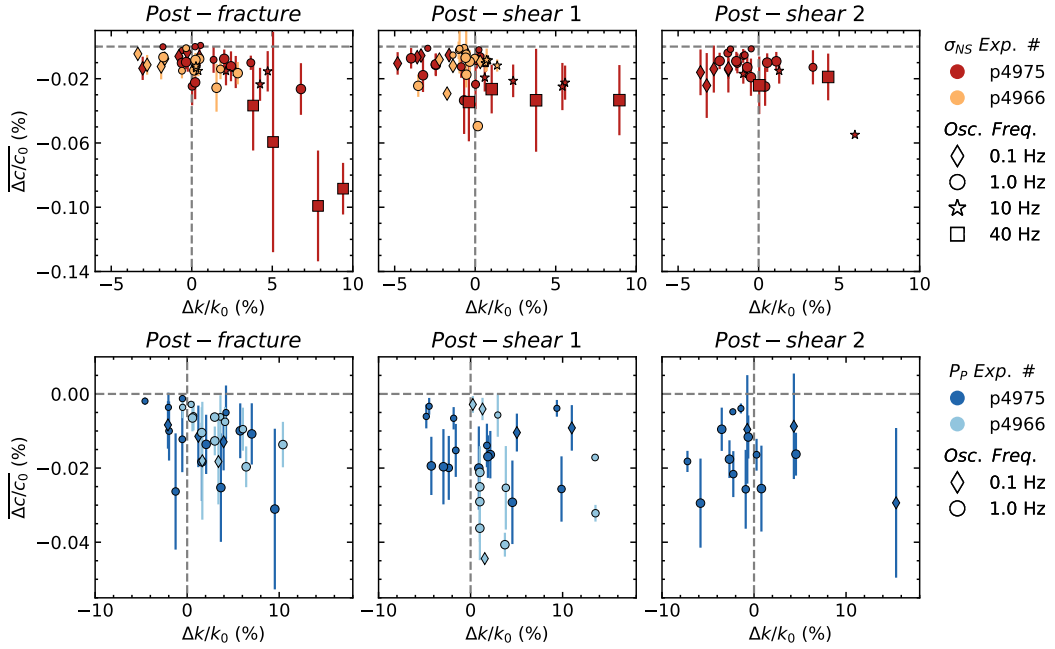


Figure 11. Nonlinearity as a function of permeability change for σ_{NS} and P_P oscillations averaged over all receivers. Data point shapes correspond to the oscillation frequencies and their sizes to amplitude. In post-fracture oscillation sets, relative changes in permeability and wave velocity are correlated. That is to say, larger normal stress or pore pressure oscillation amplitude and frequencies produce larger transient softening and permeability enhancement. Overall, shear weakens this relationship, reducing the amount of nonlinearity and permeability enhancement for both methods of dynamic stressing.

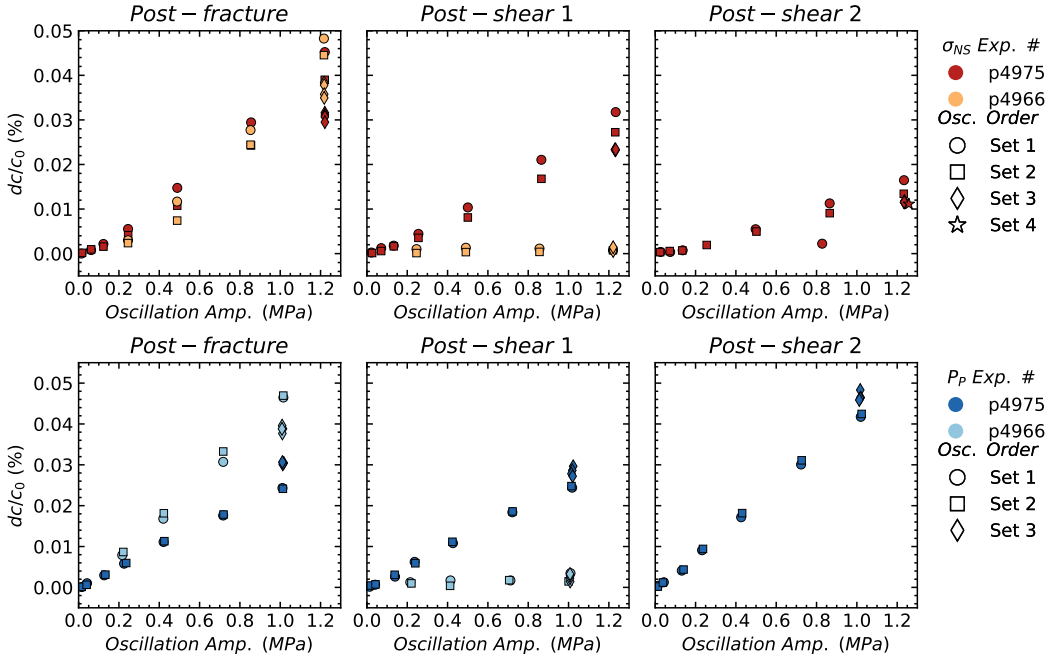


Figure 12. Velocity amplitude modulation averaged over all receivers (dc/c_0) as a function of normal stress and Pore pressure oscillations. There is a systematic reduction in dc/c_0 with accumulated shear for normal stress oscillations and there is very little variation in the oscillation order. The results from pore pressure oscillations in p4966 tell a similar story as the normal stress oscillations, but the pore pressure oscillations in p4975 show no change from post-fracture to post-shear 1 and an increase in dc/c_0 from post-shear 1 to 2.

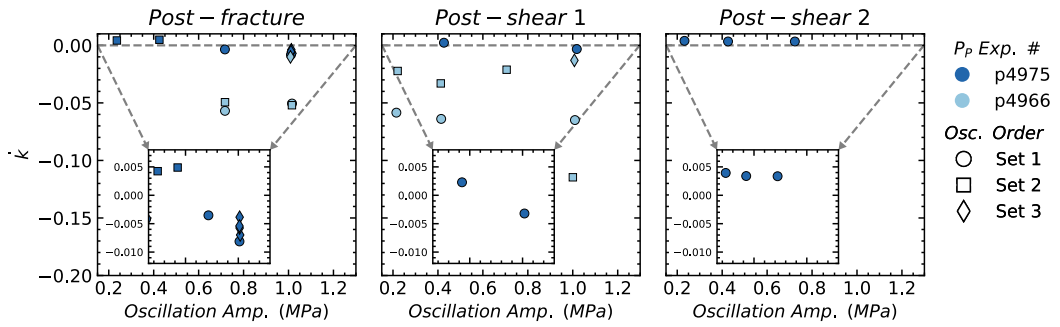


Figure 13. Permeability recovery \dot{k} as a function of applied stress oscillations for P_P . Data point shapes indicate oscillation order. Recovery rate \dot{k} linearly decreases with P_P oscillation amplitude in p4975 and subsequent shearing results in slower \dot{k} for P_P oscillations.

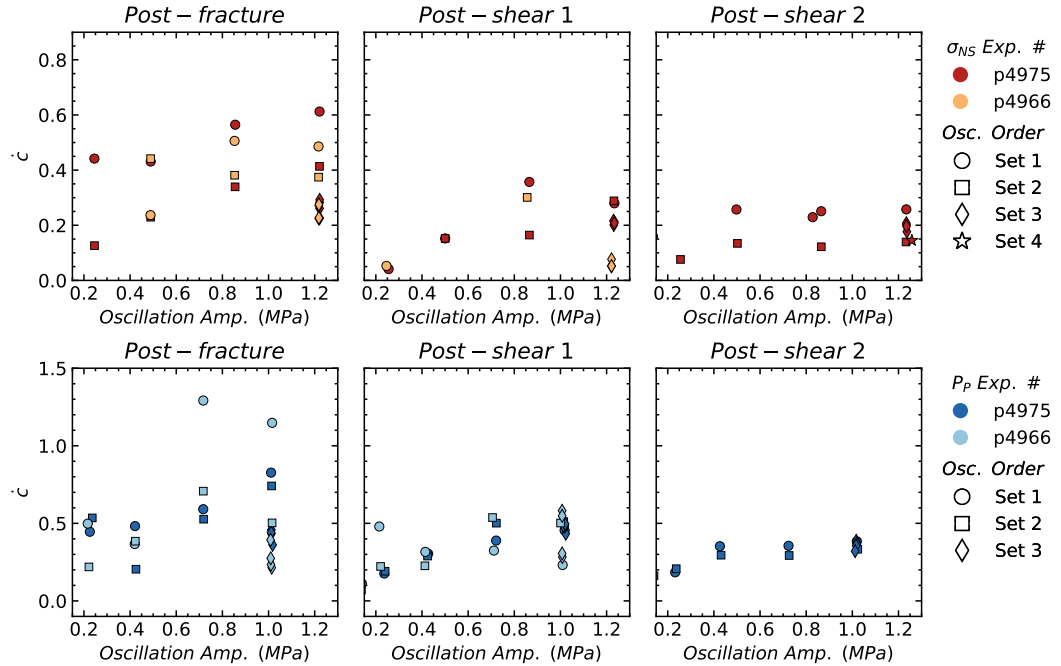


Figure 14. Wave velocity recovery \dot{c} for direct-path receiver as a function of applied stress oscillations for σ_{NS} and P_P . Data point shapes represent oscillation order. The recovery rate \dot{c} modestly increases with both σ_{NS} and P_P . Shearing decreases \dot{c} and flattens after the second shear displacement.

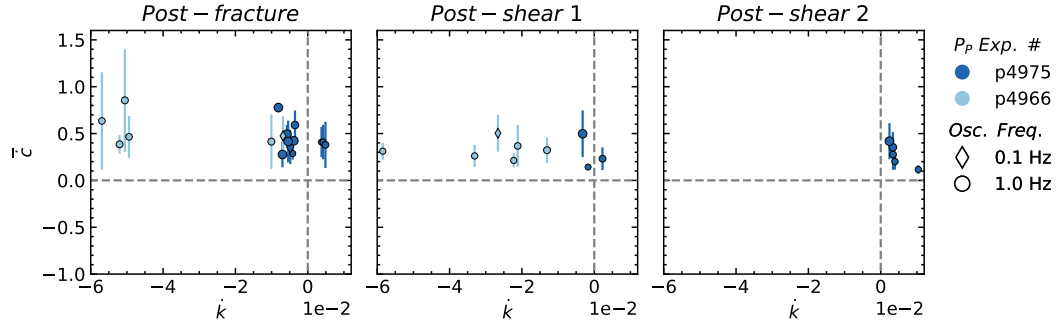


Figure 15. Wave velocity recovery rate \dot{c} as a function of permeability recovery rate \dot{k} for P_P oscillations averaged over all receivers. Data symbol shapes correspond to the oscillation frequencies and their sizes to amplitude. In post-fracture oscillation sets, both high frequency and large amplitude oscillations yield faster recovery rates for both velocity and permeability. The predominant effect of shearing is a significant reduction in \dot{k} for σ_{NS} oscillations, but increase for P_P oscillations.